This figure "f1.gif" is available in "gif" format from:

This figure "f2.gif" is available in "gif" format from:

This figure "f3.gif" is available in "gif" format from:

This figure "f4.gif" is available in "gif" format from:

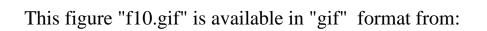
This figure "f5.gif" is available in "gif" format from:



This figure "f7.gif" is available in "gif" format from:

This figure "f8.gif" is available in "gif" format from:

This figure "f9.gif" is available in "gif" format from:



This figure "f11.gif" is available in "gif" format from:

This figure "f12.gif" is available in "gif" format from:

This figure "f13.gif" is available in "gif" format from:

This figure "f14.gif" is available in "gif" format from:

Ultraviolet Imaging of the Irregular Galaxy NGC 4449 with UIT: Photometry and Recent Star-Formation History

Robert S. Hill^{1,2}, Michael N. Fanelli^{1,2}, Denise A. Smith³, Ralph C. Bohlin³, Susan G. Neff², Robert W. O'Connell⁴, Morton S. Roberts⁵, Andrew M. Smith², Theodore P. Stecher²

ABSTRACT

The bright Magellanic irregular galaxy NGC 4449 was observed during the Astro-2 Space Shuttle mission by the Ultraviolet Imaging Telescope (UIT), which obtained images of a 40' field centered on the galaxy in two broad far-ultraviolet (FUV) bands centered at 1520 Å and 1620 Å, with 3'' - 5'' spatial resolution. Together with $H\alpha$ and $H\beta$ fluxes from ground-based Fabry-Perot images, these data are analyzed in order to explore the recent star formation history of NGC 4449. Maps of the flux ratios $H\alpha/FUV$ and FUV/blue continuum are presented and interpreted using evolutionary synthesis models. Photometry is presented both for 22 apertures containing large OB complexes and for 57 small apertures containing compact FUV-emitting knots. The OB complexes along the northern edge of the visible system have high $H\alpha/FUV$ ratios, and thus appear to be more dominated by the current generation of stars than are other parts of the galaxy. However, young sources do exist elsewhere and are particularly conspicuous along the bar. The small aperture analysis shows three candidate regions for sequential star formation. Surface brightness profiles are consistent with an exponential disk in both the FUV and the optical continuum.

Subject headings: galaxies: individual (NGC 4449) — galaxies: irregular — galaxies: photometry — galaxies: stellar content — ultraviolet: galaxies

¹Raytheon STX Corp., Code 681, NASA/Goddard Space Flight Center, Greenbelt, MD 20071

²Laboratory for Astronomy and Solar Physics, Code 681, NASA/GSFC, Greenbelt, MD 20771

³Space Telescope Science Institute, 3700 San Martin Dr., Baltimore, MD 21218

⁴University of Virginia, P.O. Box 3818, Charlottesville, VA 22903

⁵National Radio Astronomy Observatory, Edgemont Rd., Charlottesville, VA 22903

1. Introduction

The bright, nearby irregular galaxy NGC 4449 is a superb target for observation at FUV wavelengths ($\lambda \lesssim 2000$ Å). As observed with broad-band filters, the morphology of NGC 4449 consists of large OB association complexes against a smooth background. The surface brightness peaks at a distinct nucleus. Balmer emission-line observations show that the OB complexes are embedded in a welter of ionized filaments (Sabbadin et al. 1984). Both the ionized and the neutral gas show interesting morphology. The innermost HI system, corresponding to the optically bright part of the galaxy, has roughly the form of a ring $\sim 5'$ in diameter (Hunter & Gallagher 1989). At greater radii, NGC 4449 is surrounded by a vast HI halo with a diameter of $\sim 2^{\circ}$, including a number of long, almost straight, armlike filaments (Hunter et al. 1998). Because of such traits, NGC 4449 has been studied frequently in recent years.

The type given for NGC 4449 in the *Third Reference Catalogue of Bright Galaxies* (RC3; deVaucouleurs et al. 1991) is IBm (barred Magellanic irregular), and that given in the *Revised Shapley-Ames Catalog* (RSA; Sandage & Tammann 1981) is SmIV (low-luminosity, very late spiral). The distance adopted for this paper is 5.4 Mpc (Kraan-Korteweg & Tammann 1979). NGC 4449 is well-suited observationally for the investigation of stellar and interstellar structures on scales of 10² to a few 10³ pc, which correspond to angular distances of a few arcsec up to several arcmin.

An earlier paper (Hill et al. 1994; Paper I) described an FUV image of NGC 4449 made with a sounding-rocket telescope (flight 36.068GG from White Sands) and compared it to optical images taken in narrow bands with the Goddard Astronomical Fabry-Perot Imaging Camera (GAFPIC; formerly known as GFPI). The GAFPIC data included both $H\alpha$ and $H\beta$, as well as nearby continuum bands. Paper I discussed in detail the relationship between continuum and emission-line images, both in a qualitative, morphological sense, and quantitatively. In particular, the ratio of $H\alpha$ to FUV emission in 22 OB association complexes was used to investigate recent star formation history, by means of association ages computed from evolutionary synthesis models of young stellar populations. However, the spatial resolution and photometric precision of the FUV data were degraded somewhat by a detector malfunction. Both for this reason and because of the short duration of the suborbital observation (126 s), it was decided to reobserve NGC 4449 using UIT.

The UIT observation was carried out in March, 1995, during the Astro-2 mission of the Space Shuttle *Endeavour* (STS-67). The deepest UIT exposure (B1 filter, 987 s) reaches a limiting FUV surface brightness fainter than $\sim 2 \times 10^{-18}$ ergs cm⁻² s⁻¹ Å⁻¹ arcsec⁻², which is $\lesssim 20\%$ of that reached by the sounding rocket image. The spatial resolution of this image is $\sim 5''$, comparable to the rocket image. However, another UIT image (B5 filter, 493.5 s)

has a better resolution of 3" because of the shorter exposure, since slight trailing occurred during the observation sequence.

All of the UIT images have a smoother, more sharply peaked, and better determined PSF than the rocket image, because the rocket data, taken with a multi-anode microchannel array (MAMA) detector, required image reconstruction from time-tagged photon events to compensate for the combined effects of severe trailing and of electronics damage at launch. For the same reason, the flat fielding of the reduced UIT images is superior. Also, the UIT observational program included a planned suite of calibration observations, whereas the rocket calibration was based on archival *IUE* spectra of objects in the science image; hence, the calibration of the UIT images is better determined.

Although we have new FUV data, the optical data used in this paper are the same as those reported in paper I. However, comparison to other H α photometry (Mayya 1994) resulted in finding a mistake in the calibration used in Paper I. Therefore, we present new photometry in optical bands as well as FUV, with recomputed ages for the OB complexes. In addition, we extend the analysis given in Paper I. First, we present color maps showing the spatial distributions of two flux ratios: H α /FUV, and FUV/optical continuum. Second, we analyze the H α /FUV ratios of 57 FUV-bright knots \sim 100 pc in diameter, smaller than the large OB complexes measured in Paper I. Integrated photometry and surface photometry are also presented.

The contents of this paper are as follows: §1,introduction; §2, observations; §3, morphology, integrated photometry, flux ratio maps, and surface photometry; §4, aperture photometry and star formation history; §5, conclusions.

2. Observations

2.1. Overview

UIT is a 38 cm Ritchey-Chrétien reflector with two separate UV-sensitive detectors, selectable by a rotating pick-off mirror. Each detector is an image tube coupled to Eastman Kodak II-aO film by fiber optics; the FUV camera has a CsI photocathode, and the near ultraviolet (NUV) camera has a Cs₂Te photocathode. The observations discussed in this paper are in two of the FUV bands, i.e., B1 (CaF₂ filter, $\lambda = 1520$ Å, $\Delta\lambda = 350$ Å) and B5 (SrF₂ filter, $\lambda = 1620$ Å, $\Delta\lambda = 220$ Å). The B1 and B5 bandpasses differ mainly at the short-wavelength cutoff, which is 1300 Å for B1, and 1460 Å for B5. B1 has the higher throughput, but it is useful only during orbital night, because the bandpass includes strong OI airglow lines (e.g., Blair et al. 1991; Waller et al. 1995). B5 is useful both for orbital

daytime and for emphasizing CIV emission.

UIT Astro-2 data reduction includes digitization with a microdensitometer, adjustment of film fog level, linearization with a characteristic curve, and flat fielding. Astrometry is done for fields where enough FUV-emitting field stars are available. This paper uses the final version of the UIT Astro-2 data reduction pipeline, which is called by the name FLIGHT22. Detailed descriptions of the UIT instrument and data reduction are given elsewhere (Stecher et al. 1997; Stecher et al. 1992). The Astro-2 UIT calibration is based on 75 measurements of 49 stars that have been observed by IUE. UIT fluxes are tied to the Finley IUE calibration (Finley & Koester 1993), which is similar to the calibration for the final IUE archive, known as NEWSIPS (Nichols & Linsky 1996). Error in tying UIT to IUE is $\sim 10\%$ (Landsman 1997).

Our observations of NGC 4449 are listed in Table 1. The UIT images were obtained using the FUV camera during the Astro-2 mission; the NUV camera failed at launch. In this paper, the 986 s B1 image and the 493.5 s B5 image are discussed. Before analysis, a sky value of 9.13×10^{-20} ergs s⁻¹ cm⁻² Å⁻¹ arcsec⁻² is subtracted from the B1 image (orbital night) and 2.60×10^{-18} ergs s⁻¹ cm⁻² Å⁻¹ arcsec⁻² from the B5 image (orbital day). Surface brightness can be expressed in monochromatic magnitudes using the formula $\mu = -2.5 \log(f_{\lambda}/A) - 21.1$, where f_{λ} is the mean flux per pixel and A is the area of a pixel in arcsec². In these units, the B1 sky is 26.50 mag arcsec⁻², and the B5 sky is 22.86 mag arcsec⁻².

NGC 4449 was observed from the ground using GAFPIC (Brown et al. 1994). These observations, made by K.-P. Cheng, R. Oliversen, and P. M. N. Hintzen, were described in detail in Paper I. The GAFPIC data consist of Fabry-Perot emission-line images at $H\alpha$, $H\beta$, and nearby continuum wavelengths with bandwidths of 20-25 Å. Hereafter, the continuum in a narrow band near $H\beta$ is called *blue*, and near $H\alpha$, red. $H\alpha$ and $H\beta$ always refer to the continuum-subtracted data.

2.2. Calibration Changes in Earlier Data

A systematic error in the rocket FUV fluxes in Paper I was discovered through a comparison with UIT data. Although the cause of the discrepancy was not determined, one possibility was a mistake in the coordinates logged in the *IUE* observing records for the archival spectra used for calibration. These spectra, SWP 5663 and LWP 4908, were supposed to be of the nucleus of NGC 4449; however, we conjecture that the actual target may have been another bright knot 0.5 to the south. In any case, the effect of the error was

to make the FUV fluxes too high by a factor of ~ 2 . The corrected rocket calibration is consistent with that for an earlier flight using the same detector (Smith et al. 1992).

Many of the arguments of Paper I relied on the $H\alpha/FUV$ flux ratio. Coincidentally, the FUV calibration error was nearly canceled in this ratio by a similar error in the $H\alpha$. The plausibility of the combined results hindered the discovery of both problems. In fact, all of the optical fluxes reported in Paper I were a factor of 1.7 too high, because an incorrect aperture diameter was applied to the HII region HK11 (Kennicutt 1988), whose $H\alpha$ flux was the calibration standard.

The corrected calibration of the GAFPIC data has been confirmed by comparison to another study that also uses HK11 as the calibration source (Mayya 1994). Also, the GAFPIC images have been refined by subtracting ghost images reflected from the Fabry-Perot blocking filter. The effect of the ghosts on the photometry of bright sources is negligible, and the main result of making the correction is to remove faint false sources from the sky 1'-2' west of the galaxy bar. Other aspects of the GAFPIC data reduction that were described in Paper I are not detailed again here, e.g., the correction for NII contamination and for the radially varying central wavelength of the Fabry-Perot sensitivity curve. However, we note that the continuum to be subtracted from the line+continuum images is scaled using foreground stars, and that H β is calibrated relative to H α using the HII region spectroscopy of Lequeux et al. (1979).

The combined calibration errors resulted in values of the $\text{H}\alpha/\text{FUV}$ flux ratio for individual OB complexes in Paper I that were too small by $\sim 20\%$. The significance of this ratio was that in combination with evolutionary synthesis models, it gave a so-called instanteous-burst (IB) age for each source. The systematic error in this age resulting from the calibration was ~ 0.5 Myr. Since the range of ages found was 0-10 Myr, a 0.5 Myr shift does not invalidate the arguments presented in Paper I on relative ages and morphology. However, the calibration does affect the global star formation rate (SFR). Moreover, because the UIT data have better flat fielding and S/N than the rocket data, we have used the UIT data to produce a complete revision of the photometric results for the 22 OB complexes (§4.1.2). The interpretation in terms of star formation history, while consistent with that in Paper I, is restated here in a more precise way, using four bandpasses.

2.3. Extinction

To correct for foreground extinction, we use the functional form of the extinction curve given by Cardelli, Clayton & Mathis (1989) with the parameter R_V set to 3.1; hereafter, the term Galactic in reference to extinction always means this curve. $H\alpha/H\beta$ ratios are converted to reddenings using the formula $E(B-V) = -1.00 + 2.184 \log(H\alpha/H\beta)$, which is computed from the Galactic curve.

To correct for extinction within NGC 4449, we use the algorithm of Calzetti (1997). This procedure is based on studies of extinction in starburst galaxies, in which the $\text{H}\alpha/\text{H}\beta$ ratio of the excited gas is compared to the ultraviolet spectral slope of the associated stellar component (Kinney et al. 1994; Calzetti, Kinney, & Storchi-Bergmann 1994; Gordon, Calzetti & Witt 1997).

The Calzetti algorithm begins with the computation of a Balmer decrement for each source. The reddening $E(B-V)_g$ of the ionized gas is computed directly from the Balmer decrement using the Galactic extinction curve. $E(B-V)_g$ is multiplied by 0.44 to obtain $E(B-V)_s$, which is the reddening of the associated stars. Broad-band continuum fluxes attributable to the stellar component are corrected in the FUV using $E(B-V)_s$ with a "starburst" extinction curve, for which Calzetti (1997) gives a functional form. This extinction curve is similar to ones found for the LMC, except that it lacks a 2200Å bump. Optical emission-line fluxes arising from the gas are corrected using $E(B-V)_g$ with the Galactic extinction curve.

In most of this paper, the single value $E(B-V)_g=0.43$, including both foreground and internal extinction, is adopted for all of NGC 4449. This value is the mean of Balmer-decrement reddenings computed for the OB complexes analyzed both in Paper I and in this paper below (§4.1). In order to avoid the influence of any error in sky or continuum subtraction in the low-surface-brightness portions of the H β image, the Balmer decrements are computed only from the bright pixels. For each aperture separately, the histogram of H α fluxes of the pixels is computed. The 95th percentile is found, and the pixels brighter than that value are used in both H α and H β to compute the Balmer decrement (Paper I). A set of 22 reddenings results, one for each large aperture, and the mean of this set is adopted as the value for NGC 4449. The scatter among the 22 values is $\sigma = 0.1$ mag.

The Galactic foreground reddening is estimated to be E(B-V)=0.03, computed by applying the dust-to-gas ratio of Bohlin, Savage, & Drake (1978) to the HI column density near the line of sight from Stark et al. (1992). Therefore, $E(B-V)_g$ in NGC 4449 is 0.40 and $E(B-V)_s$ is 0.18.

The mean Balmer decrement reddening E(B-V)=0.43 can be compared with values

from other authors. Martin (1997) tabulates several logarithmic extinctions at H β in NGC 4449. Converted to E(B-V), these values are 0.07, 0.5, and 0.2 for diffuse ionized gas and 0.03 and 1.2 for HII regions. Spectra in an effective aperture of $3' \times 2'$ were obtained by Kennicutt (1992) using a drift scan. From the resulting Balmer decrement, we compute E(B-V) = 0.47. In summary, our value appears to be in the appropriate range.

Our justification for using the Calzetti algorithm is that in conjunction with evolutionary synthesis models, it yields fairly consistent SFRs over several timescales, each of which is based on a different bandpass. This analysis and the influence of the extinction law are described below ($\S4.1.2$).

3. Global Properties of NGC 4449

3.1. Morphology and Integrated Photometry

NGC 4449 is surrounded by a neutral hydrogen halo extending to as far as $\sim 1^{\circ}$ from the visible system, reaching in projection the neighbor galaxy DDO 125, as shown by an Effelsberg 100-meter map (Bajaja, Huchtmeier, & Klein 1994). The corresponding VLA map (Hunter et al. 1998) shows that this gas is highly structured, with linear streamers and tails $\sim 30''$ long. The UIT images show no UV-emitting counterpart to the HI halo, so that within a 20' radius of the galaxy center, star formation appears to be confined to the well-known features of the visible galaxy.

Subimages of the UIT frames of NGC 4449 are compared with optical data in Figure 1. Following Hodge & Kennicutt (1983), the origin of the coordinate system is one of the four foreground stars seen in the optical images. The UIT images are on the left, and the blue and H α images are on the right. Both the FUV and the optical bands show bright knot complexes against a relatively faint, but still evident, background. However, the morphology of the background depends on whether it is observed in broad-band continuum or in line emission. In the H α image, the background is intricately structured and comprises numerous ionized filaments, but in the FUV and blue continuum images, the background is relatively smooth and diffuse. Figure 2 shows a contour map of the B1 image. The lowest contour plotted, which is that for a surface brightness 1.3×10^{-17} ergs cm⁻² s⁻¹ Å⁻¹ arcsec⁻², encloses almost all of the galaxy, including the diffuse component.

The FUV-emitting knot seen in the western part of the UIT subimages in Figure 1 lies outside the field of view of the optical data. The region between this isolated knot and the main body of the galaxy contains X-ray emitting gas (Della Ceca, Griffiths & Heckman 1997). A ring or torus of neutral hydrogen is coincident with the galaxy in projection

(Hunter & Gallagher 1989). The eastern side of the ring, which has a broken, somewhat chaotic morphology in H_I, coincides with the main body of the galaxy, and the western side of the ring coincides with the isolated FUV knot.

Conspicuous in NGC 4449 at all of our observed wavelengths are the sites of recent star formation, which are found in the apparent bar of NGC 4449, as well as in the armlike extensions to the north and south. Note that the bar of NGC 4449 is different from those found in barred spiral galaxies, as shown by the K-band surface brightness profile (Thronson et al. 1987).

The FUV and B absolute magnitudes of NGC 4449 are compared with those of several other galaxies in Table 2. The FUV magnitudes are preliminary measurements from the UIT Galaxy Atlas (Fanelli et al. 1998, in preparation), and the B magnitudes are from the RSA. NGC 4449 is bright for a Magellanic irregular, though not extreme (Hunter et al. 1998), and it is of comparable brightness to some spirals. In broad-band continuum magnitudes, both FUV and optical, NGC 4449 is intrinsically 2-3 times as bright as the LMC.

The intrinsic FUV-B color of NGC 4449 implied by Table 2 is -1.43. This value can be compared to the UV-B colors of RC3 galaxies observed by the FAUST ultraviolet telescope (Figure 2 of Deharveng et al. 1994), where UV \approx 1600Å. The result is that NGC 4449 is near the mean color for FAUST irregulars.

An important indicator of an unusual history for NGC 4449 is the gas kinematics, which several studies show to be peculiar, both in the central, bright system and in the extended HI envelope. By peculiar, we mean primarily that the observed motions are clearly inconsistent with a single rotating disk. The velocity gradient along the major axis in the inner, optically bright part is in the opposite sense to the rotation of the outer HI system (Sabbadin et al. 1984; Malumuth, Williams, & Schommer 1986). On a local scale, sharp velocity gradients are seen within the bright ionized gas, and the resulting shocks are a possible stimulus for star formation (Hartmann, Geller, & Huchra 1986).

3.2. Flux Ratio Maps

3.2.1. General Interpretation

Flux ratio maps have considerable heuristic value in the study of galaxies. Continuum ratios can show spatial patterns both of star formation and of dust, because the slope of the aggregate spectrum is reddened either by extinction or by the aging of the stellar

population. Ratios involving emission lines can show how the excitation processes in the interstellar medium are distributed in relation to stars. Here, we investigate NGC 4449 using two ratio maps, $H\alpha/B1$ and B1/blue continuum.

An important tool for analyzing flux ratio maps, as well as the aperture photometry described later in this paper, is evolutionary synthesis modeling. Fluxes from a cluster (or any coeval group) of stars are computed by a weighted sum of contributions from various model atmospheres. The weighting is derived from an assumed initial mass function (IMF); in this paper, we use a Salpeter power law slope, which may be expressed as $\gamma = -2.35$, $\Gamma = -1.35$, or Γ

3.2.2. $H\alpha/B1$

Although FUV and H α images both show the locations of early-type stars, they do not show exactly the same stars. In a zero-age population, H α is emitted by interstellar gas photoionized by early- to mid-O stars, whereas FUV is emitted by stars over a somewhat broader range of spectral types from O to early B. The masses of the stars that dominate ionizing flux, $N_{\rm Lyc}$, and the 1500 Å continuum, L_{150} , have been computed for a Salpeter IMF extending up to 110 M_{\odot} by means of the evolutionary synthesis models, with the following results: at zero-age, 90% of $N_{\rm Lyc}$ is contributed by stars with $M/M_{\odot} > 30$ and lifetime less than ~ 7 Myr, and 90% of L_{150} is contributed by stars with $M/M_{\odot} > 12$ and lifetime less than ~ 30 Myr. Hence, OB associations from 7 to 30 Myr old should be much brighter in FUV than in H α images, provided that they were formed in single bursts of star formation and no current generation of high-mass stars exists to contribute ionizing flux.

Even for OB associations less than 7 Myr old, $N_{\rm Lyc}$ and L_{150} decline at different rates, so that the ratio of H α to FUV surface brightness can be used as a clock. Unfortunately, evolutionary synthesis models cannot give this flux ratio directly, because the configuration of the gas and dust that surround each OB association is typically unknown. However,

simplifying assumptions can be made. The models used in this paper incorporate the following assumptions: (1) HII regions are ionization bounded; (2) extinction of the ionizing continuum by dust within HII regions is negligible; (3) extinction outside the HII regions is described by the starburst reddening model of Calzetti (1997) (§2.3).

Of these three assumptions, the first is known to be inaccurate. Leakage of ionizing photons from NGC 4449 HII is estimated at $\sim 20\%$ (Hunter & Gallagher 1992); moreover, in a study of the transition from HII regions to diffuse ionized gas, Martin (1997) finds no clear boundary between these two domains. If the leakage is consistent over all of the HII regions, the sequence of relative ages computed from $H\alpha/FUV$ ratios will not be significantly affected. The zero-point shift resulting from the detection of only 80% of ionizing flux is ~ 0.5 Myr. The second assumption, that of low internal extinction in the HII regions, is consistent with the Calzetti method of extinction correction, which implies that the extinction is caused primarily by dust in a shell configuration, i.e., dust that lies in front of the sources rather than being mixed with them (Gordon, Calzetti & Witt 1997).

Figure 3 plots the logarithm of the theoretical $N_{\rm Lyc}/{\rm B1}$ ratio vs. age, computed from the IB models as described above. The Y axis on the right-hand side shows the observable quantity ${\rm H}\alpha/{\rm B1}$ that results if E(B-V)=0.43 is applied as described above (§2.3). This plot can be compared with the grayscale map in Figure 4, which shows the spatial distribution of the observed $H\alpha/{\rm B1}$ ratio. Before taking the quotient, the ${\rm H}\alpha$ image is smoothed with a Gaussian of FWHM 3".6 to match the B1 resolution.

The black areas in Figure 4 correspond to IB ages of ≤ 4 Myr. We emphasize that the delta-function star formation history is unlikely to be a good approximation for every source, particularly in interpreting the optical continuum, but it does give a convenient measure of domination by short-lived stars as compared to stars with lifetimes of a few 10^7 yr. The northeast periphery of NGC 4449, at the upper left of the image, is clearly the most active region of the galaxy in terms of the dominance of current over past star formation. In the rest of the galaxy, smaller star-forming regions are interspersed with areas of relative quiescence, which are light in the image. The two most conspicuous of these areas are at coordinates (0.7, 0.9) and (1.0, -0.6). The first area appears in Figure 4 as a white crescent in the upper-right quadrant of the galaxy, and it coincides exactly with an OB association seen in Figure 1. This source is an example of an association whose age is $\gtrsim 7$ Myr, with values of log H α /B1 $\approx 0.4 - 0.45$. The second area appears in Figure 4 as a compact white spot in the southern bar of the galaxy. Here, the lowest-valued pixels in log $H\alpha/B1$ are ~ 0.25 , corresponding to an IB age of ~ 11 Myr. Immediately to the west is a conspicuous knot of current star formation. It is tempting to speculate that sequential star formation (SSF) has occurred in this region, proceeding from east to west ($\S4.2$).

A possible alternative explanation for the high ${\rm H}\alpha/{\rm B1}$ ratios is extinction, which would preferentially suppress the FUV. A difference in Balmer decrement reddening of $\Delta E(B-V)=+0.1$ increases log ${\rm H}\alpha/{\rm B1}$ by 0.1-0.2, depending on the extinction model, with the Calzetti starburst model at the low end of this range and the Galactic extinction curve at the high end. Thus, variations of this size could result from neglected variation in E(B-V), since we use an average value. However, the range of values seen in Figure 4 is much greater, ± 0.8 in log ${\rm H}\alpha/{\rm B1}$. This question is considered in greater detail below (§4.1.2).

3.2.3. B1/Blue

A plot of the B1/blue ratio from an aging OB association is shown in Figure 5. This flux ratio is computed from IB models as described above; for comparison, an $\text{H}\alpha/\text{B1}$ model is also shown. The left-hand Y axis gives unreddened ratios, and the axes on the right give the ratios as reddened by our average extinction model (§2.3). The corresponding map of the B1/blue ratio observed in NGC 4449 is shown in Figure 6. To match resolutions, the blue is smoothed with a Gaussian of FWHM 3″.6, then a residual difference in PSF shape is removed by smoothing both images with a Gaussian of FWHM 2″.3. Dark areas have a high B1/blue ratio and therefore represent stars relatively young on the average. The spatial variations are fairly smooth, and the map is dominated by broad features of order ~ 0 ′.5 in diameter, a few times the smoothed resolution.

Of interest in Figure 6 is the absence of any strong features corresponding either to the nucleus of NGC 4449 (coordinates 0.8, -0.1; cf. Figure 1) or to two FUV sources that lie ~ 0.3 arcmin to the northeast of the nucleus. The H α image and the H α /B1 ratio image show that star formation is happening currently in these knots. However, they are in the bar, which has the highest broad-band surface brightness at all wavelengths. Most likely, this region is the site of frequent star formation episodes and has a historically high mean star formation rate, as compared to the periphery. As a result, relatively recent star formation in the bar fails to outweigh older generations of stars in the continuum flux ratio map, whereas at larger radii, star formation episodes are infrequent, and one recent generation can outshine the older stars left from previous episodes.

Hunter & Gallagher 1990 show that the northern periphery of NGC 4449 coincides with an H_I cloud, which may feed the star formation.

3.3. Radial Profiles

The radial surface brightness profile of NGC 4449 is shown in Figure 7 in both the UIT B1 band and the narrow red continuum band. The red profile appears to be exponential. The B1 profile is lumpy, because of the bright star-forming complexes, which reflect local conditions in the interstellar medium; however, it appears approximately exponential except in the center, where a cusp is seen in both the optical and the FUV.

A similar analysis has been done with UIT data for the irregular galaxy NGC 4214 (Fanelli et al. 1997). These authors find that NGC 4214, otherwise similar to NGC 4449, shows a deVaucouleurs profile in the FUV out to a radius of ~ 3 kpc. They argue that because this profile is characteristic of dynamically hot systems, a merger may have played an important role in causing the recent star formation in the central region of NGC 4214. Although a merger scenario has been suggested in order to explain the peculiar gas kinematics in *both* NGC 4449 and NGC 4214 (Hartmann, Geller, & Huchra 1986), NGC 4449 outside the nucleus appears to be dominated by a star-forming disk.

3.4. Froth

The term froth has been coined to describe a certain morphology of H α -emitting material outside typical HII regions. Froth lacks conspicuous embedded OB complexes, and it is distinguished from simple diffuse emission by a complex structure of bright filaments. The froth is thought to be the product of a mixed ionization mechanism, with energy supplied mostly by ionizing stars, but also by shocks (Hunter & Gallagher 1990; Hunter & Gallagher 1997).

A plausibility argument for the importance of photoionization can be made with a simple application of the FUV image data. We examine the ratio between H α surface brightness in any given local area and the coincident FUV surface brightness. If the ratio of H α to FUV is consistent with that expected from an ionizing cluster, then photoionization is a plausible mechanism. Apertures $\sim 20''$ in radius are superposed on 4 regions of diffuse, filamentary H α emission and extended FUV emission (Figure 8). The H α and FUV fluxes for these regions are given in Table 3, together with $\log N_{\rm Lyc}/L_{\rm B1}$, without extinction corrections or background flux subtraction. These values all fall within a range consistent with IB cluster models, i.e., consistent with photoionization by young stars. The FUV surface brightnesses are equivalent to ~ 1 late B star per pc², as computed using a standard UV stellar library (Fanelli et al. 1992). However, this number represents a lower limit, because of extinction. An argument based on H α emission measures gives an estimate of

ionizing flux equivalent to 1 early B star per pc² in some of the H α structures in NGC 4449 (Hunter & Gallagher 1990).

More recently, a detailed spectroscopic analysis (Hunter & Gallagher 1997) has shown that $H\alpha$ froth structures on all size scales are dominated by photoionization. The largest filaments are widely separated from the main stellar component of NGC 4449, so that their photoionization requires Lyc photons to traverse kpc-scale paths from the nearest OB associations. However, the four regions measured here are embedded in the luminous body of the galaxy, so that it is not clear whether the ionization is caused by the conspicuous OB associations or by dispersed B stars.

4. Recent Star-Formation History

4.1. Large Apertures

4.1.1. Recapitulation of Previous Analysis

In Paper I, an FUV sounding-rocket image was used together with the GAFPIC emission-line imagery to compute ages for emission knots in 22 large apertures of irregular shape with diameters $\sim 0.2-0.5$, each enclosing a complex of OB associations and HII regions. After correcting for extinction and converting H α to $N_{\rm Lyc}$ using case B recombination (Osterbrock 1989), the log of the ratio $N_{\rm Lyc}/L_{\rm FUV}$ provided a measure of the age via an IB model of an evolving cluster. It was found that individually, both the numerator and denominator declined rapidly after zero-age, so that the ratio was dominated by the youngest stars included. Therefore, the modeled IB age gave, to some degree of approximation, the age of the most recent generation of stars within each photometric aperture.

Photometry of the large apertures showed high ${\rm H}\alpha/{\rm FUV}$ ratios for a group of sources arranged in an arrowhead or bow-wake shape along the northern periphery of NGC 4449, coinciding with an HI cloud. The IB model showed that the age difference from the OB complexes in the bar was ~ 2.5 Myr. The question was whether this was a significant result. In other words, could one conclude that the northern part of NGC 4449 was undergoing a coherent star formation event, separated in time from the most recent star formation in the bar?

In order to answer this question, Paper I investigated whether differences in star formation history could perturb the IB age so that it failed to give the age of the latest generation of stars, and instead was contaminated by previous generations. The conclusion

was that this effect could occur. An IB model with age t Myr gave the same value of $\log N_{\rm Lyc}/L_{\rm FUV}$ as a model of CSF beginning at the formation of the galaxy and stopping t-2 Myr ago. The application to the age difference between the north and the bar was this: if we applied the IB model to the north and the CSF model to the bar, then the age difference became ~ 0.5 Myr for the youngest generation, which was not significant. The age difference was preserved only if we could assume the same type of star formation history for both regions. However, the difference in morphology and surface brightness between the north and the bar made it seem possible that two different histories did apply.

Therefore, the interpretation of Paper I ended in a disjunction. Either of two interesting results could be true, but the data and simple models could not decide between them. Either the north and the bar had the same type of star formation history, and the latest generation of stars was younger in the north; or else the latest generation of stars was the same age in both regions, but they had different prior star formation histories. Paper I chose the second interpretation as more likely. In either case, the sources measured in the north differed from those in the bar in a way that was manifested in the observed ${\rm H}\alpha/{\rm FUV}$ ratio.

4.1.2. New Analysis Including UIT Data

Table 4 gives the positions and sizes of the 22 large apertures defined in Paper I. These apertures are used for photometry of both the UIT B1 data and the recalibrated GAFPIC data. The large apertures are shown in Figure 9; each encloses one major complex of OB associations. The main result of Paper I was a tendency for the knots in the bar region to have greater IB ages than those in the outlying regions along the northern edge of the galaxy by 2-3 Myr. Generally, this trend is confirmed.

A discussion of the systematic errors in the large-aperture analysis was given in Paper I. Many potential problems were considered, e.g., poor scaling of continuum images to line+continuum images or poor sky subtraction. In general, such errors result in shifts of a few 0.1 Myr in the entire IB age scale, with little effect on the sequence of ages in the galaxy.

A few details of the flux determinations and the models are as follows:

- 1. No background flux internal to NGC 4449 is subtracted, since this procedure was shown in Paper I to have little effect on the IB ages.
- 2. Extinction is computed for each bandpass using the algorithm of Calzetti (1997),

described above ($\S 2.3$).

3. For simplicity, the IB models are computed with an initial mass function (IMF) over the range $0.1-110~\rm M_{\odot}$ with a Salpeter slope, whereas a multi-component IMF was used in Paper I.

The photometric results are given in Table 5, in which the columns are as follows: (1) ordinal number or object name; (2) location: N for the northern part of the galaxy, B for the bar, and O for other areas; (3) logarithm of the spectral irradiance (flux) in the UIT B1 band in ergs cm⁻² s⁻¹ Å⁻¹; (4) logarithm of the irradiance in the H β line in ergs cm⁻² s⁻¹; (5) H β equivalent width in Å (no background within NGC 4449 subtracted); (6) logarithm of the irradiance in the H α line in ergs cm⁻² s⁻¹; (7) H α equivalent width in Å (no background within NGC 4449 subtracted); (8) color index computed from the UIT B1 band and the narrowband continuum at 4830 Å, respectively, in magnitudes (same f_{λ} zero point for both bands); (9) color index computed from the narrowband continuum at 4830 Å and 6520 Å, respectively, in magnitudes (same f_{λ} zero point for both bands); (10) age in Myr computed from log $N_{\text{Lyc}}/L_{\text{B1}}$ using the IB cluster model.

Internal errors in FUV fluxes are $\sim 1-3\%$; those in optical fluxes are mostly less than 1%, except for a few H β measurements with errors of 5 – 7%. The internal errors in the age, computed by propagating the photometric errors through extinction correction and the IB model, are less than 0.1 Myr, except for sources 1, 3, 7, 15, 19, 20, 21, and 22, which have errors of 0.1 – 0.4 Myr.

The IB ages inferred from the ratio $H\alpha/B1$ are depicted in a bar chart in Figure 10. Again, the youngest OB association complexes in terms of IB models are in a group located along the northeastern edge of the galaxy. For reference, a 2.5 Myr difference in IB age requires $H\alpha/B1$ ratios to differ by a factor of 3.

The observed B1/blue flux ratio for the large apertures is plotted vs. H α emission equivalent width, denoted EW(H α), in Figure 11, where the apertures are classified by their location in the galaxy into the categories *north* (triangles), *bar* (squares), and *other* (plusses). Both the plotted quantities decrease with age. All but one of the northern apertures lie to the upper right of the plot, with log B1/blue> 0.7 and EW(H α)> 110Å, i.e., where both H α and FUV are strong compared to the optical continuum.

The H α /FUV ratio is interpreted in this paper as being determined by star formation history. However, two possible objections to this idea are the following: (1) differences in H α /FUV can be caused by differences in the amount of extinction, since a relatively high extinction suppresses FUV more than H α ; (2) differences in H α /FUV can be caused

by differences in the leakage of the ionizing photons from the HII regions. Figure 11 weighs against these objections. If the high values of $H\alpha/FUV$ in the north are caused by extinction, the same sources should also have low FUV/blue ratios, which is not the case. Furthermore, $EW(H\alpha)$ is a ratio of two quantities at nearly the same wavelength and thus is unaffected by reddening. One could postulate a difference in dust geometry between the sources in the north and the others. E.g., low values of the parameter $E(B-V)_s/E(B-V)_g$ could explain the high B1/blue ratios in the north, since both B1 and blue are stellar continuum; however, this would lower $EW(H\alpha)$ by raising the stellar continuum in relation to $H\alpha$. Finally, although variations in ionizing flux leakage could explain variations in $EW(H\alpha)$, the B1/blue ratio is immune to this effect.

In other words, we find a fourfold correlation between position in the galaxy, $\text{H}\alpha/\text{B1}$, B1/blue, and $\text{EW}(\text{H}\alpha)$, which is evidence for a real difference between regions. Certainly, it is possible to find complex hypotheses that would explain these correlations without invoking age or star formation history. E.g., the extinction curve in the north could be flatter than in the bar, thus causing B1/blue to be higher in the north, and this effect could be combined with a large difference in ionizing flux leakage. Nevertheless, such a scenario is significantly more subtle than the two simple objections noted above. Surely, the either/or interpretation at the end of §4.1.1 offers the best working hypothesis.

If, indeed, the difference in IB model age between the north and the bar is mainly caused by a difference in the *type* of star-formation history, i.e., IB vs. CSF, then this interpretation is compatible with that offered by Hunter (1997) that star formation has occurred over a long period of time in the periphery of NGC 4449, just as it has in the bar, but with relatively infrequent and distinct episodes, of which the present episode is one instance.

Using various photometric bands, the average star formation rate (SFR) over a timescale appropriate for each band is computed for the whole galaxy from CSF models. This timescale is given by a flux-weighted mean of the ages of IB models, as follows:

$$\langle t \rangle_{\lambda} = \frac{\int_0^{\infty} t L_{\rm IB}(\lambda, t) dt}{\int_0^{\infty} L_{\rm IB}(\lambda, t) dt} \text{Myr},$$

where $L_{\rm IB}(\lambda,t)$ is the luminosity at a given wavelength computed using the IB model for age t Myr. The results are given in Table 6 (cf. Table 6 of Paper I). Each row is for one bandpass and its associated timescale, given in the first two columns. Each of the three columns labeled ZERO, CALZ, and GAL, respectively, gives the results of a different method of extinction correction. The SFR values under ZERO have no correction for extinction within NGC 4449, those under CALZ are corrected using the Calzetti (1997) method for the NGC 4449 component as described in §2.3, and those under GAL are

corrected by using the Galactic curve for both the NGC 4449 and foreground components.

Table 6 shows that the SFR over last few 10^7 yr (UIT B1 band) is the most sensitive to the extinction correction of the three timescales considered. Both the ZERO and the CALZ results are fairly consistent over the three timescales; however, the extinction in NGC 4449 is substantial, and a correction is needed, so the SFR values under ZERO are rejected. The GAL method is simple, but it produces an apparent ~ 5 —fold peak in the SFR $\sim 10^7$ yr ago, because of the strong enhancement in the derived FUV fluxes with respect to H α and blue continuum. This alone is not sufficient reason to reject the method, since such an enhancement might occur. Nevertheless, we provisionally adopt the scenario of consistent SFRs as the more likely one and for that reason, we use the Calzetti (1997) extinction-correction method. In Paper I, the same goal was achieved by an *ad hoc* use of the Orion Nebula extinction curve, which has a shallow FUV rise (Bohlin & Savage 1981).

The extinction-corrected H α photometry can be used to compare sources in NGC 4449 to the local standard for bright HII regions, 30 Dor. The value of $L_{\rm H}\alpha$ adopted for 30 Dor is $10^{40.2}$ ergs s⁻¹ (Conti 1991). With an extinction of E(B-V)=0.43 and a distance of 5.4 Mpc, this value becomes $10^{-11.76}$ ergs s⁻¹ cm⁻², where we use the Galactic extinction curve. Comparison with Table 5 shows that only one large aperture includes a greater H α luminosity than 30 Dor, i.e., aperture 18, which encloses a complex region in the southern part of the bar, containing several clusters and H α shells. Let $n_{\rm 30D,H}\alpha$ be the number of 30 Dor units of H α flux emitted by a given source. Then, for aperture 18, $n_{\rm 30D,H}\alpha=1.9$; for large aperture 6, which includes the brightest compact HII region in NGC 4449, $n_{\rm 30D,H}\alpha=0.8$; for the whole of NGC 4449, $n_{\rm 30D,H}\alpha=11.5$. For the LMC itself, if we adopt an H α luminosity of 4.1×10^{40} ergs s⁻¹ (Kennicutt & Hodge 1986), then $n_{\rm 30D,H}\alpha\approx2.5$.

4.2. Small Apertures

The UIT B5 image has spatial resolution of $\sim 3''$, equivalent to a projected distance of ~ 80 pc in NGC 4449. In the LMC, this size is of the same order as the diameter of a small OB association (Lucke & Hodge 1970). Accordingly, compact knots consisting of a few resolution elements in the B5 image of NGC 4449 can be treated reasonably as coeval OB associations. Although this assumption is unlikely to be strictly accurate (Garmany 1994), it is both commonly applied and difficult to avoid in OB association studies.

We compute ages for our small associations from $H\alpha/B5$ flux ratios in circular apertures. The definition of apertures is done with a program that displays the B5 and the $H\alpha$ images side by side. A circular aperture is overplotted on each image and sized

interactively. The purpose of the simultaneous sizing is to try to define a single aperture containing associated stars and gas in both bands. A background annulus around each aperture is also defined simultaneously for both images in the same way. The resulting apertures are overplotted on the B5 image in Figure 12 and on the H α image in Figure 13. The numbers are shown in Figure 14, and the locations and sizes are given in Table 7.

The goal in defining the small apertures is to characterize the compact, bright FUV sources seen within larger structures, such as the bar, the northern "arms," and the southern extensions. We include mainly sources that are bright and in good contrast against the background in both bands; but some sources that are bright in only one band are included if they are in the immediate neighborhood of sources seen well in both bands. E.g., sources 17, 18, and 20 are conspicous in the B5 image and faint in $H\alpha$, whereas the reverse is true of source 41, yet all of these sources are included because they are part of larger structures that include several other measurements. However, a number of compact HII regions are both relatively isolated and lacking a distinct counterpart in the B5 image, and so they are omitted.

Compact FUV sources in several external galaxies have been analyzed in WF/PC imagery by Meurer et al. (1995), who investigate the distribution of star formation in central starburst galaxies and conclude that super star cluster formation is $\sim 20\%$ a of the total SFR. Unfortunately, the UIT resolution does not permit a direct comparison of our results to those achieved with WF/PC. The sources of Meurer et al. (1995) have diameters of order ~ 10 pc and in many cases less, in contrast to the 80 pc limit imposed by the resolution of our B5 image. Moreover, we infer typical 2200 Å absolute magnitudes $-16 \gtrsim M_{220} \gtrsim -18$ for our small apertures, based on the color B5–220 ≈ -0.9 for a 4 Myr old IB model. These values are 1-2 mag brighter than most of those in the WF/PC study, showing again that our small sources are more likely to be associations than clusters. However, the real size and morphology of these sources cannot be determined from the UIT data.

Background subtraction within NGC 4449 is a difficult problem because of crowding and surface brightness gradients. Accordingly, we do not apply the background annuli individually to the particular sources they surround, but instead, we use them in a more complex procedure. The sources are divided into groups, each of which appears likely to have a common background value. Each background annulus is broken up into octants, and all the octants for a group of sources are treated together, regardless of which source each octant was originally associated with.

The photometry program integrates the fluxes for each aperture and for each background octant. Each of these fluxes is separately corrected using its own Balmer

decrement with the method described above (§2.3). The collection of octants for each group of sources is sorted, and the 3/8 of the collection with the lowest values are selected. The mean of these lowest values is adopted as the background for the group of sources, and the standard error of the mean is adopted as the error in the background.

The photometric and modeling results are given in Table 8, in which the columns are as follows: (1) ordinal number of source; (2) group membership, with each group assumed to have a single, common value of background flux; (3) logarithm of the spectral irradiance in the UIT B5 band in ergs cm⁻² s⁻¹ Å⁻¹; (4) logarithm of the irradiance in the H β line in ergs cm⁻² s⁻¹; (5) logarithm of the irradiance in the H α line in ergs cm⁻² s⁻¹; (6) $E(B-V)_g$ in magnitudes, including Galactic foreground; (7) logarithm of the inferred ionizing photon luminosity in photons s⁻¹; (8) logarithm of the inferred spectral luminosity in the B5 band in ergs s⁻¹ Å⁻¹; (9) IB age in Myr as computed from the H α /B5 ratio (the value $< \theta$ means that log $N_{\rm Lyc}/L_{\rm B5}$ is greater than the range covered by the models); (10) estimated error in age in Myr; (11) note, encoded as follows: Bn, H β background less than zero; Un, FUV background less than zero; Bx, source flux less than zero in H β .

As a check of the photometry, we have looked for a correlation between the E(B-V) values of all the sources and their IB ages, to see whether the age variation merely reflects errors in the reddening estimates, because of the leverage of the FUV rise in the extinction correction, but no such correlation is found.

Background fluxes less than zero are subtracted from the flux of the source just like ones greater than zero, so that a minus background raises the flux of the source; such cases are assumed to have resulted from a correction for continuum and overall sky that is too great in the particular region. However, source fluxes less than zero are omitted from subsequent analysis.

Internal errors in the raw small aperture fluxes are typically $\sim 6\%$ for B5, $\sim 1\%$ for H α , and $\sim 3\%$ for H β . The maximum errors found for individual sources are 20% for B5, 5% for H α , and 13% for H β . Error in the background value for each set of grouped small apertures contributes significantly to the total photometric error. The resulting error in the age estimate is computed from the following propagation-of-error formula:

$$\sigma^{2}(\text{age}) = 7.49(\sigma(F_{\text{H}\alpha})/F_{\text{H}\alpha})^{2} + 31.39(\sigma(F_{\text{H}\beta})/F_{\text{H}\beta})^{2} + 8.17(\sigma(f_{\text{B5}})/f_{\text{B5}})^{2}.$$

This formula takes into account the adopted extinction correction method and the dependence of the computed extinction on $H\alpha$ and $H\beta$, and it uses an approximate linear fit to the model trace shown in Figure 3. The $H\alpha$ contributes less to the total error than either of the other measurements, because it enters the computation twice, in ways that cancel. With other values held constant, an increase in $H\alpha$ leads to an increase in age via

the extinction correction, which raises the FUV flux, but the same increase in H α leads to a decrease in age directly via the IB model.

The correspondence between small and large apertures is given in Table 9, together with the IB age and stellar reddening $E(B-V)_s$ (§2.3) for each small aperture. In most cases, the large-aperture age is at least as great as the youngest small-aperture age in the corresponding group, as expected if the compact sources contain the youngest stars. However, for large apertures 1, 7, 15, 18, 21, and 22, this relationship does not hold, i.e., the large-aperture age is less than at least one corresponding small-aperture age by 1 Myr or more. For large apertures 7 and 18, the reason may be crowding of compact sources. For large aperture 15, the individual compact sources are aging OB assocations and are probably a minor source of the ionizing flux that causes the surrounding $H\alpha$ emission. Large apertures 1, 21, and 22 contain diffuse filamentary $H\alpha$ features, and thus account better for the ionizing flux than do the small apertures.

A related analysis of stellar generations uses FUV spectra taken with the $10'' \times 20''$ aperture of IUE (Home et al. 1995; Home 1997). The pointings correspond to our large apertures 6, 10, 14, 16, 18, 19, and 21. The analysis is an evolutionary synthesis different from the one done in this paper, in that it is based on a grid of binned high-resolution IUE stellar spectra. The fitting depends primarily on age-sensitive spectral features, and allows either one or two age components. These results show evidence for multiple generations in the age range 0-12 Myr at 5 of the 7 positions. The youngest mean age is given by large aperture 6, consistent with our results. Typically, the IUE ages are ~ 3 Myr greater than our corresponding large-aperture ages. Reddenings E(B-V) within NGC 4449 of a few 0.01 are found by fitting the *IUE* spectra of the OB associations with moderately steep, LMC or 30 Dor extinction curves (Home 1997). These reddenings are lower than the values $E(B-V)_s = 0.44E(B-V)_g$ in our small apertures at the same positions by $\Delta E(B-V) \approx 0.1$. Hence, the IUE analysis is consistent with $E(B-V)_s < E(B-V)_q$. Taken at face value, our results imply that the proportionality constant between $E(B-V)_s$ and $E(B-V)_g$ is less than 0.44; however, the apertures are not matched between the two sets of data.

Figure 14 shows a map of our compact source ages, with outlines emphasizing 3 regions that show a spatial progression of ages. These patterns may indicate sequential star formation (SSF; Elmegreen & Lada 1977; Home 1997). In this scenario, the typical spatial separation between stellar generations appears to be $\sim 100-300$ pc, a factor of 5 larger than in Elmegreen & Lada's Galactic examples. In the FUV-brightest region of the southern bar (1.0, -0.5 in Figure 14, corresponding to large aperture 18 in Figure 9), we measure 6 sources, with a progression of ages from the west (young, sources 41 and 43) to

the east (old, source 45). Sources 43 and 45 lie approximately along an east-west line with a separation of 0'.13, or 204 pc. The age difference of 8.3 Myr implies a propagation speed of 25 km s⁻¹, which is larger than the canonical sound speed of 10 km s⁻¹ for 8000 K HII regions (Spitzer 1978); however, this speed is less than that of an associated ionized shell (40 km s⁻¹), and in the same range as other shells in NGC 4449 (Hunter & Gallagher 1990). This group is physically the most likely case of SSF, as the distances between generations are relatively small, and the propagation velocity is moderate. Moreover, a double H α shell emanating from this group toward the east, at coordinates (0.9, -0.6) in Figure 13, is suggestive of multiple, discrete star formation episodes.

In the northwest "arm" of NGC 4449, a group of 9 sources shows a progression of ages from west (young, sources 12 and 14) to east (old, sources 17 and 22). Small apertures 14 and 17, with an age difference of 10.4 Myr, are separated by 756 pc, implying a propagation speed of 73 km s⁻¹. A different pattern is seen in the center of the galaxy, where a line of young associations (33, 34, 38, 39, 47, 49, and 50), parallel to the bar, lies \sim 0′.3 east of the older associations along the ridgeline (31, 32, 36, 37, 45). The propagation speed between these two lines would be \sim 70 – 100 km s⁻¹.

Models of propagating star formation in NGC 4449 are computed by Home 1997. The models are of two types: "short-range," in which propagation is by the ionization-shock front of an expanding HII region, and "long-range," in which propagation is by wind- and supernova-blown bubbles. The long-range case is more relevant to our observations. Here, the propagation is modeled in two phases: a bubble is pressurized by winds and supernovae for 3 Myr, then begins an adiabatic free expansion, which continues until the surrounding shell fragments. The expansion velocity of the bubble after the first phase is an upper limit on the total propagation speed. The outcome of the models is that this limit is in the range $20 - 50 \text{ km s}^{-1}$ for the 7 *IUE* pointings described above, comparable to that of shell velocities observed in NGC 4449 (Hunter & Gallagher 1990).

A few other instances of possible SSF outside our Galaxy are found in the literature. One recent example is from an infrared study of the center of M82 (Satyapal et al. 1997), where a linear arrangement of clusters with approximately ordered ages extends over a distance of ~ 230 pc. The implied propagation speed is ~ 50 km s⁻¹, consistent with the gas motions in that environment. A smaller-scale example is the OB associations LH 9 and LH 10 in the LMC (Parker et al. 1992), which are $\sim 5'$ apart, or ~ 70 pc for a distance modulus of 18.48 (Westerlund 1997). Although the authors do not commit themselves to a definite value for the age difference between the two associations, from the upper mass limits of their color-magnitude diagrams, it appears to be small, ~ 1 Myr or less, using the Geneva stellar evolution tracks (Schaerer et al. 1993). The implied propagation speed is

 $\sim 70 \ {\rm km \ s^{-1}}.$

In summary, in some regions of NGC 4449, the OB associations appear to be arranged spatially in an approximate order of age. In two of the three cases discussed above, the implied propagation speeds are somewhat higher than typical measured H α shell velocities in NGC 4449, though within a factor of 2 of apparent propagation speeds seen in other galaxies. On the other hand, the region of large aperture 18 contains the most likely instance of propagating star formation, as the velocity of propagation would be in the range expected for the motion of expanding ionized shells.

5. Conclusions

Color maps in $H\alpha/FUV$ and FUV/blue continuum show variation in these ratios over the galaxy. The northern tier of HII regions shows a generally high $H\alpha/FUV$ ratio compared to the rest of the galaxy. The regions of high FUV/blue ratio coincide with outlying OB complexes, but the OB complexes in the nuclear region, which has a high optical surface brightness, are in low contrast against the background in the FUV/blue map.

The scenario previously presented in Paper I, i.e., that the youngest UV-emitting populations are found in the northern part of NGC 4449, is reinforced. However, young associations also exist in the bar region of the galaxy. Photometry of large OB complexes is consistent with the idea of Hunter (1997) that star formation occurs continually in the periphery of NGC 4449, just as it does in the bar, but with relatively infrequent and distinct episodes.

Photometry of compact sources in small apertures shows several instances of correlation between age and spatial location, but the physical significance of these correlations is unclear. Direct propagation of star formation from one site to the next appears possible in at least one case. The implied propagation speeds are in the range $20 - 100 \text{ km s}^{-1}$.

The interpretation of FUV aperture photometry in NGC 4449 relies on the starburst extinction model of Calzetti (1997). If the consistency of average star formation rates over several time intervals is used as a constraint, then this treatment of extinction appears justified for NGC 4449.

The radial surface brightness profile in the FUV approximates an exponential disk, in contrast to the similar galaxy NGC 4214, where the FUV profile follows an $r^{1/4}$ law. The ratio of diffuse FUV flux to H α flux in the smooth, extended component of NGC 4449 is consistent with photoionization.

Thanks to Bill Waller for commenting on the manuscript. Thanks to Allen Home for a copy of his informative thesis. The authors are grateful to all those on board the Shuttle for both Astro-1 and Astro-2, as well as to the engineers and technicians who made these missions possible. Funding for the UIT project has been through the Spacelab Office at NASA Headquarters under project number 440-51. R. W. O. was supported in part by NASA grants NAG 5-700 and NAGW-2596 to the University of Virginia.

REFERENCES

Bajaja, E., Huchtmeier, W. K., & Klein, U. 1994, A&A, 285, 385

Bessell, M. S. 1979, PASP, 91, 589

Blair, W. P., et al. 1991, ApJ, 379, L33

Bohlin, R. C. & Savage, B. D. 1981, ApJ, 249, 109

Bohlin, R. C., Savage, B. D., & Drake, J. F. 1978, ApJ, 224, 132

Bothun, G. D. 1986, AJ, 91, 507

Brown, L. W., Woodgate, B. E., Ziegler, M. M., Kenney, P. J., & Oliversen, R. J. 1994, Rev. Sci. Instrum., 65, 3611

Calzetti, D. 1997, in The Ultraviolet Universe at Low and High Redshift, eds. W. H. Waller, M. N. Fanelli, J. E. Hollis, & A. C. Danks (Woodbury: AIP), p. 403

Cardelli, J. A., Clayton, G. C., & Mathis, J. S. 1989, ApJ, 345, 245

Calzetti, D., Kinney, A. L., & Storchi-Bergmann, T. 1994, ApJ, 429, 582

Conti, P. S. 1991, in Massive Stars in Starbursts, C. Leitherer et al. eds., (Cambridge: CUP), p. 21

Deharveng, J.-M., Sasseen, T. P, Buat, V., Bowyer, S., Lampton, M., & Wu, X. 1994, A&A, 289, 715

de Vaucouleurs, G., de Vaucouleurs, A., Corwin, H. G., Buta, R. J., Paturel, G., & Fouque, P. 1991, Third Reference Catalogue of Bright Galaxies (Springer: New York) (RC3)

Della Ceca, R., Griffiths, R. E., & Heckman, T. M. 1997, ApJ, 485, 581

Elmegreen, B. G. & Lada, C. J. 1977, ApJ, 214, 725

Fanelli, M. N. et al. 1997, ApJ, 481, 735

Fanelli, M. N., O'Connell, R. W., Burstein, D., & Wu, C.-C. 1992, ApJS, 82, 197

Finley, D. S., & Koester, J., private communication

Garmany, C. D. 1994, PASP, 106, 25

Gordon, K. D., Calzetti, D., & Witt, A. N. 1997, ApJ, 487, 625

Hartmann, L. W., Geller, M. J., & Huchra, J. P. 1986, AJ, 92, 1278

Hill, R. S., Cheng, K.-P., Bohlin, R. C., O'Connell, R. W., Roberts, M. S., Smith, A. M., & Stecher, T. P. 1995, ApJ, 446, 622

Hill, R. S., Home, A. T., Smith A. M., Bruhweiler, F. C., Cheng, K.-P., Hintzen, P. M. N., & Oliversen, R. J. 1994, ApJ, 430, 568

Hodge, P. & Kennicutt, R. C., Jr. 1983, An Atlas of H II Regions in 125 Galaxies, PAPS Document ANJO88-296-300 (NY: AIP Auxiliary Publication Service)

Home, A. T., Bruhweiler, F. C., Neubig, M. S., Hill, R. S., & Landsman, W. 1995, BAAS, 27, 1355

Home, A. T. 1997, unpublished Ph. D. dissertation, Catholic University of America

Hunter, D. A. 1997, PASP, 109, 937

Hunter, D. A. & Gallagher, J. S. 1989, Science, 243, 1557

Hunter, D. A. & Gallagher, J. S. 1990, ApJ, 362, 480

Hunter, D. A. & Gallagher, J. S. 1992, ApJ, 391, L9

Hunter, D. A. & Gallagher, J. S. 1997, ApJ, 475, 65

Hunter, D. A., Wilcots, E. M., van Woerden, H., Gallager, J. S., & Kohle, S. 1998, ApJ, 495, L47

Kennicutt, R. C., Jr., 1988, ApJ, 334, 144

Kennicutt, R. C., Jr., 1992, ApJ, 388, 310

Kennicutt, R. C., Jr., & Hodge, P. W. 1986, ApJ, 306, 130

Kinney, A. L., Calzetti, D., Bica, E., & Storchi-Bergmann, T. 1994, ApJ, 429, 172

Kraan-Korteweg, R. C. & Tammann, G. A. 1979, Astron. Nach., 200, 181

Kurucz, R. L. 1991, in The Stellar Populations of Galaxies, ed. B. Barbuy & A. Renzini (Dordrecht: Kluwer), 225

Landsman, W. L. 1997, private communication

Lequeux, J., Peimbert, M., Rayo, J. F., Serrano, A., & Torres-Peimbert, S. 1979, A&A, 80, 155

Lucke, P. B., & Hodge, P. W. 1970, AJ, 78, 171

Malumuth, E. M., Williams, T. B., & Schommer, R. A. 1986, AJ, 91, 1295

Martin, C. L. 1997, ApJ, 491, 561

Mayya, Y. D. 1994, AJ, 108, 1276

Meurer, G. R., Heckman, T. M., Leitherer, C., Kinney, A., Robert, C., & Garnett, D. R. 1995, AJ, 110, 2665

Nichols, J. S., & Linsky, J. L. 1996, AJ, 111, 517

Osterbrock, D. E. 1989, Astrophysics of Gaseous Nebulae and Active Galactic Nuclei (Mill Valley: University Science Books)

Parker, J. W., Garmany, C. D., Massey, P., & Walborn, N. 1992, AJ, 103, 1205

Sabbadin, F., Ortolani, S., & Bianchini, A. 1984, A&A, 131, 1

Sandage, A. S. & Tammann, G. A. 1981, A Revised Shapley-Ames Catalog of Bright Galaxies, (Washington: Carnegie) (RSA)

Satyapal, S. et al. 1997, ApJ, 483, 148

Schaerer, D., Meynet, G., Maeder, A., & Schaller, G. 1993, A&AS, 98, 523

Smith, A. M., Cornett, R. H., & Hill, R. S. 1987, ApJ, 320, 609 (erratum, ApJ, 355, 746)

Smith, A. M., Hill, R. S., Vrba, F. J., & Timothy, J. G. 1992, ApJ, 391, L81

Spitzer, L., Jr., 1978, Physical Processes in the Interstellar Medium (New York: Wiley), p. 227

Stark, A. A., Gammie, C. F., Wilson, R. W., Bally, J., Linke, R. A., Heiles, C., & Hurwitz, M. 1992, ApJS, 79, 77

Stecher, T. P. et al. 1992, ApJ, 395, L1

Stecher, T. P. et. 1997, PASP, 109, 584

Thronson, H. A., Jr., Hunter, D. A., Telesco, C. M., Harper, D. A., & Decher, D. 1987, ApJ, 317, 180

Westerlund, B. 1997, The Magellanic Clouds (Cambridge: CUP), p. 147

Waller, W. H. et al. 1995, AJ, 110, 1255

This preprint was prepared with the AAS IATEX macros v4.0.

- Fig. 1.— Ultraviolet and ground-based images of NGC 4449 (see Table 1). North is up and east to the left, with coordinates in arcmin. Power-law gray scaling with index 0.3. UIT images in broad FUV bands (B1 and B5) are on the left, and GAFPIC images in narrow optical bands are on the right. B1 and B5 have mean wavelengths of 1521Å and 1615Å, respectively, for a flat input spectrum. Blue is the off-band continuum at 4830Å, near H β . H α is continuum-subtracted. Four foreground stars are seen in the optical data at (-1.6, -0.8), (-1.6, 1.4), (-0.8, -1.7), and (0,0); these are imperfectly subtracted in the H α image because of a slight PSF mismatch.
- Fig. 2.— Contour map of UIT FUV Image of NGC 4449 in the B1 Band. North is up and east to the left, with coordinates in arcmin. In units of 10^{-17} ergs cm⁻² s⁻¹ Å⁻¹ arcsec⁻², the contour levels are 1.3, 3.9, 11.6, 34.8, and 104.5.
- Fig. 3.— IB cluster models used to derive ages of UV and H α sources. A Salpeter IMF is assumed with mass limits $0.1M_{\odot}$ and $110M_{\odot}$. Abscissa: time since the formation of a coeval group of stars. The left-hand ordinate axis gives the log of the ratio of the ionizing photon luminosity (photons s⁻¹) to the FUV luminosity (ergs s⁻¹). The right-hand ordinate axis gives the log of the observable ratio H α /B1 assuming our average extinction model (§2.3).
- Fig. 4.— Map of log H α /B1. North is up and east to the left, with coordinates in arcmin. Flux ratio scaling from log H α /B1 of 0.2 (white; less H α) to 1.6 (black; more H α); the actual range of values in the galaxy is 0.25 1.98. H α is smoothed by a Gaussian of FWHM 3".6. To remove sky noise, H α values are clipped at 1.6 × 10⁻¹⁶ ergs cm⁻² s⁻¹ arcsec⁻², and B1 at 2.2 × 10⁻¹⁷ ergs cm⁻² s⁻¹ Å⁻¹ arcsec⁻². See Figure 1 for coordinates of foreground stars.
- Fig. 5.— IB cluster evolution models, aged from 1 Myr to 1 Gyr. A Salpeter IMF is assumed with mass limits $0.1M_{\odot}$ and $110M_{\odot}$. Dashed line: log of ratio of H α flux to FUV flux in the UIT B1 band; solid line: log of ratio of B1 to blue continuum. Right-hand ordinate axes give observable ratios H α /B1 and B1/blue assuming our average extinction model (§2.3).
- Fig. 6.— Map of log B1/blue. North is up and east to the left, with coordinates in arcmin. The flux ratio scaling is from log B1/blue of 0.04 (light; less UV) to 1.5 (dark; more UV). The actual range of values in NGC 4449 is -0.29 to +1.25. Light circles are foreground stars. The blue (4830 Å) is smoothed with a Gaussian of FWHM 3".6, then both images are additionally smoothed with a Gaussian of FWHM 2".3. To remove sky noise, B1 values are clipped at 2.6×10^{-17} ergs cm⁻² s⁻¹ Å⁻¹ arcsec⁻², and blue at 9.6×10^{-18} ergs cm⁻² s⁻¹ Å⁻¹ arcsec⁻².
- Fig. 7.— Surface brightness profiles of NGC 4449 in the UIT B1 band and in the 6520 Å narrow red continuum band. Abscissa: mean radius of annular aperture in arcsec, or 0.5

the radius of the central circular aperture. Ordinate: log of the surface brightness in units of ergs cm⁻² s⁻¹ Å⁻¹ arcsec⁻². Outside the central cusp, the r band fits an exponential profile except for a hump at a radius of $\sim 100''$, due to the bright star-forming complex at the northern edge of the galaxy. Photometric errors are given by the error bars for B1 and are less than the size of the symbols in r.

- Fig. 8.— Froth regions marked on continuum-subtracted GAFPIC H α map; photometry is given in Table 3. North is up and east to the left, with coordinates in arcmin. See Figure 1 for coordinates of foreground stars, which are imperfectly subtracted because of a slight PSF mismatch.
- Fig. 9.— UIT FUV Image of NGC 4449 in the B5 band. North is up and east to the left, with coordinates in arcmin. Logarithmically scaled. Large apertures from Paper I are indicated (Table 4). Sources are classified as follows according to the region of the galaxy in which they are found. North: 1, 2, 4, 5, 6, 7, 9, 13, 15, 17, 19; bar: 8, 10, 11, 12, 14, 16, 18; other: 3, 20, 21, 22.
- Fig. 10.— Bar chart showing IB ages computed from B1 and H α fluxes in large apertures (Table 5). Abscissa: large aperture number. Ordinate: age in Myr. Region of the galaxy where the sources are located is encoded in shading of the bars as given by legend (cf. Figure 9). The youngest 6 sources are along the northeastern edge of the galaxy.
- Fig. 11.— Plot of log B1/blue vs. equivalent width in H α for large aperture measurements with no extinction corrections. Plot symbols signify region of the galaxy as in Table 5 and Figure 9: triangles, north; squares, bar; plusses, other.
- Fig. 12.— Small apertures on the UIT B5 image. North is up and east to the left, with coordinates in arcmin. Apertures are defined manually by adjusting them simultaneously on B5 and H α images. Cf. Figure 13. Aperture positions and sizes are given in Table 7; numbering and modeled ages are given in Figure 14. Image is log scaled, and pixel values are clipped to be greater than a surface brightness of 1.6×10^{-17} ergs cm⁻² s⁻¹ Å⁻¹ arcsec⁻².
- Fig. 13.— Small apertures on the H α image. North is up and east to the left, with coordinates in arcmin. Apertures are defined manually by adjusting them simultaneously on B5 and H α images. Cf. Figure 12. Aperture positions and sizes are given in Table 7; numbering and modeled ages are given in Figure 14. Image is log scaled, and pixel values are clipped to be greater than a surface brightness of 1.6×10^{-16} ergs cm⁻² s⁻¹ arcsec⁻².
- Fig. 14.— Small aperture ages on the UIT B5 image. North is up and east to the left, with

coordinates in arcmin. Numbers are as in Tables 7 and 8. Symbols denote ages in Myr, as follows: 0-3, triangles; 3-5, squares; 5-7, plusses; >7, crosses. Source 55, which does not have a measurable H β flux, is included in the oldest category. Outlines emphasize regions where ages are in approximate sequence. E.g., ages decrease from east to west starting with source 45.

Table 1: Observations
Table 2: Comparison of Absolute Magnitudes
Table 3: Photometry of Froth Regions
Table 4: NGC 4449 Large Apertures
Table 5: Photometry in Large Apertures
Table 6: Global Star Formation Rates
Table 7: NGC 4449 Small Apertures

Table 8: Photometry in Small Apertures

Table 9: Correspondance of Large and Small Apertures

TABLE 1
OBSERVATIONS

Instrument	Image	Bandpass	Exp.Time (s)	Date
UIT	FUV2229	B1	986.7	1994 Mar 7
	FUV2230	B1	98.2	1994 Mar 7
	FUV2231	B5	493.5	1994 Mar 7
GAFPIC		$_{ m Hlpha}$	300.0	$1992~\mathrm{May}~27$
		$6520 { m \AA}$	300.0	1992 May 27
		$_{\mathrm{H}eta}$	500.0	1992 May 27
	•••	4830 Å	500.0	1992 May 27

TABLE 2 Comparison of Absolute Magnitudes

Galaxy	$M_{ m FUV}{}^{ m a}$	$M_B{}^{ m b}$	Type ^c
LMC	-18.8	-18.43	SBmIII
NGC 4214	-19.12	-18.79	SBmIII
NGC 4449	-20.27	-18.84	SmIV
M81	-18.34	-20.75	Sb(r)I-II
M51	-20.91	-21.60	Sbc(s)I-II
M101	-22.01	-21.51	Sc(s)I
			. ,

^aPreliminary results from UIT Galaxy Atlas, Fanelli et al., in preparation, except for the LMC, which is computed from sounding rocket data shown in Smith, Cornett, & Hill 1987. ${}^{\rm b}M_{B_T}^{0,i}$ from the RSA. ${}^{\rm c}$ From the RSA.

TABLE 3 PHOTOMETRY OF FROTH REGIONS

N	<i>X</i> (′)	<i>Y</i> (′)	r (')	$\begin{array}{c} \log \mathrm{B1^a} \\ (\mathrm{ergs} \; \mathrm{cm}^{-2} \; \mathrm{s}^{-1} \; \mathrm{\mathring{A}}^{-1}) \end{array}$	$\log H\alpha^{a}$ (ergs cm ⁻² s ⁻¹)	$\frac{\log N_{\rm Lyc}^{\rm a}}{/\log L_{\rm B1}}$
1	-0.80	-0.93	0.16	-13.6	-12.6	12.9
2	-0.46	-1.23	0.16	-13.7	-12.8	12.8
3	-0.36	-1.80	0.16	-14.0	-13.0	12.8
4	-0.22	-1.77	0.20	-13.9	-13.0	12.8

^aNo extinction corrections.

TABLE 4NGC 4449 Large Apertures

Source ^a	X^{b}	Y^{c}	$Area^d$
1	-0.95	0.51	0.13
2	-0.47	0.77	0.13
3	-0.33	-0.08	0.15
4	-0.14	0.97	0.07
5	0.07	1.39	0.07
6	0.29	1.48	0.06
7	0.34	1.28	0.03
8	0.41	-0.68	0.15
9	0.40	1.16	0.03
10	0.40	0.43	0.09
11	0.41	0.05	0.14
12	0.44	-0.30	0.08
13	0.53	1.30	0.03
14	0.69	0.19	0.05
15	0.67	0.89	0.08
16	0.79	-0.09	0.12
17	0.89	1.09	0.06
18	0.97	-0.59	0.39
19	1.15	1.16	0.06
20	1.54	0.55	0.04
21	1.57	-1.37	0.11
22	1.58	-2.14	0.19

^aSee Figure 9.

^bArcmin west as in axes of Figures 1,2,4,6,8,9, and 12-14; origin of coordinates is same foreground star as used by Hodge & Kennicutt 1983. ^cArcmin north. ^dArcmin².

TABLE 5
PHOTOMETRY IN LARGE APERTURES

Region (1)	Location (N, B, or O) (2)	$ \begin{array}{c} \log B1 \\ (ergs cm^{-2} s^{-1} Å^{-1}) \\ (3) \end{array} $	$ \begin{array}{c} \log H\beta \\ (\operatorname{ergs} \operatorname{cm}^{-2} \operatorname{s}^{-1}) \\ (4) \end{array} $	EW(Hβ) (Å) (5)		EW(Hα) (Å) (7)	15 – 48 (mag) (8)	48 - 65 (mag) (9)	Age (Myr) (10)
1	N	-14.13	-13.43	31	-12.72	129	-1.96	0.23	4.6
2	${ m N}$	-13.61	-12.84	33	-12.18	123	-1.87	0.22	4.5
3	O	-14.11	-13.77	4	-12.92	25	-0.65	0.12	5.8
4	N	-13.96	-13.06	43	-12.41	146	-1.86	0.31	3.8
5	N	-13.83	-12.83	79	-12.18	232	-2.23	0.46	3.1
6	N	-13.62	-12.53	101	-11.88	283	-2.29	0.50	2.8
7	N	-13.68	-13.24	28	-12.65	111	-2.50	-0.02	6.4
8	В	-13.42	-12.73	26	-12.12	88	-1.81	0.22	5.2
9	N	-13.78	-13.20	37	-12.58	146	-2.48	0.06	5.7
10	В	-13.28	-13.02	9	-12.37	42	-1.77	0.00	6.9
11	В	-13.09	-12.64	11	-11.99	47	-1.50	0.07	6.1
12	В	-13.68	-13.06	14	-12.41	55	-1.36	0.18	5.4
13	N	-13.89	-13.12	55	-12.48	194	-2.44	0.24	4.7
14	В	-13.44	-12.96	15	-12.33	60	-1.72	0.05	6.1
15	N	-13.37	-13.36	9	-12.70	44	-2.40	-0.04	8.3
16	В	-12.98	-12.49	11	-11.83	46	-1.35	0.06	5.9
17	N	-13.63	-12.97	58	-12.34	181	-2.75	0.33	5.3
18	В	-12.55	-12.12	15	-11.50	61	-1.89	0.04	6.4
19	N	-13.85	-13.40	48	-12.77	152	-3.07	0.32	6.2
20	O	-14.57	-14.07	17	-13.35	63	-1.84	0.40	5.6
21	O	-13.78	-13.66	8	-12.82	56	-1.96	-0.02	6.7
22	O	-13.92	-13.86	7	-12.74	92	-1.98	0.03	5.8
NGC 4449		-11.82	-11.46	9	-10.71	46	-1.52	0.14	6.1

TABLE 6 GLOBAL STAR FORMATION RATES

Banda	$(< t >)^{b}$			Extinction Corrections $(M_{\odot} \text{ yr}^{-1})$
		ZERO ^c	$CALZ^d$	$\mathrm{GAL^e}$
$H\alpha$	2.2×10^{6}	0.51	1.30	1.30
UIT B1	4.1×10^7	0.52	3.18	10.91
$4830~\textrm{\AA}$	1.9×10^9	0.43	1.66	1.66

^aFluxes in Table 2.

^bUnits are yr; flux-weighted average of ages of cluster models contributing flux at the given wavelength (§4.1.3).

^cCorrected for Galactic foreground extinction of E(B-V) = 0.03 using extinction curve of Cardelli et al. 1989 with parameter $R_V = 3.1$.

^dCorrected for E(B-V)=0.40 using extinction algorithm of Calzetti 1997 and E(B-V)=0.03 using the Galactic extinction curve of Cardelli et al. 1989 with parameter $R_V=3.1$.

^eCorrected for E(B-V)=0.43 using the Galactic extinction curve of Cardelli et al. 1989 with parameter $R_V=3.1$.

 $\begin{array}{c} \text{TABLE 7} \\ \text{NGC 4449 SMALL APERTURES} \end{array}$

N	X^{a}	$Y^{ m b}$	$r^{ m c}$
1	0.27	1.42	0.11
2	0.07	1.41	0.23
3	0.37	1.39	0.07
4	0.52	1.29	0.15
5	0.33	1.26	0.18
6	0.45	1.18	0.09
7	1.14	1.13	0.16
8	-0.33	1.09	0.13
9	0.82	1.09	0.14
10	0.90	1.03	0.10
11	0.75	0.99	0.08
12	1.18	0.98	0.10
13	-0.14	0.96	0.15
14	1.08	0.94	0.07
15	0.11	0.93	0.10
16	-0.03	0.92	0.14
17	0.60	0.92	0.08
18	0.74	0.91	0.13
19	-0.41	0.82	0.09
20	0.57	0.81	0.13
21	1.05	0.75	0.08
22	0.76	0.74	0.12
23	-0.56	0.72	0.18
24	-0.41	0.71	0.12
25	-0.02	0.58	0.09
26	-0.96	0.56	0.20
27	1.51	0.55	0.17
28	-0.81	0.52	0.15
29	0.32	0.46	0.08
30	0.47	0.45	0.15

TABLE 7—Continued

N	X^{a}	$Y^{ m b}$	r^{c}
31	0.64	0.20	0.18
32	0.54	0.04	0.1
33	0.32	0.00	0.08
34	0.43	-0.02	0.10
35	-0.32	-0.06	0.20
36	0.60	-0.06	0.13
37	0.77	-0.13	0.20
38	0.44	-0.19	0.1
39	0.51	-0.32	0.1
40	0.98	-0.34	0.0
41	1.09	-0.40	0.0
42	1.07	-0.47	0.0
43	1.14	-0.50	0.0
44	0.11	-0.53	0.0
45	1.02	-0.55	0.0
46	1.11	-0.58	0.1
47	0.49	-0.59	0.1
48	0.30	-0.63	0.3
49	0.52	-0.67	0.0
50	0.46	-0.74	0.0
51	0.81	-0.99	0.1
52	1.56	-1.33	0.2
53	1.71	-1.42	0.1
54	1.84	-1.42	0.1
55	1.20	-1.81	0.1
56	1.55	-1.96	0.1
57	1.60	-2.16	0.2

 $^{^{\}rm a} \rm See~Figures~12-14.$ $^{\rm b} \rm Arcmin~west~as~in~axes~of~Figures~1,2,4,6,8,9,~and~12-14;~ori$ gin of coordinates is same foreground star as used by Hodge & Kennicutt 1983.

CArcmin north.

 $^{^{\}rm d}{\rm Radius}$ in arcmin.

TABLE 8
PHOTOMETRY IN SMALL APERTURES

N	Group	$\begin{array}{c} \log \mathrm{B5} \\ (\mathrm{ergs} \ \mathrm{cm}^{-2} \\ \mathrm{s}^{-1} \ \mathrm{\mathring{A}}^{-1}) \end{array}$	$ \begin{array}{c} \log H\beta \\ (\text{ergs cm}^{-2} \\ s^{-1}) \end{array} $	$ \begin{array}{c} \log H\alpha \\ (\text{ergs cm}^{-2} \\ s^{-1}) \end{array} $	$\frac{E(B-V)_g}{(\text{mag})}$	$\log N_{ m Lyc} \ ({ m photons~s}^{-1})$	$ \begin{array}{c} \log L_{\rm B5} \\ ({\rm ergs\ s^{-1}}) \\ {\rm \mathring{A}^{-1}}) \end{array} $	$_{\rm (Myr)}^{\rm Age}$	$\sigma(age)$ (Myr)	Note
(1)	(2)	(3)	(4)	(5)	(6)	(7)	(8)	(9)	(10)	(11)
1	1	-14.01	-12.74	-12.09	0.43	51.73	38.30	2.3	0.1	_
2	2	-14.07	-12.94	-12.29	0.43	51.48	38.09	2.4	0.6	
3	1	-14.70	-13.75	-13.11	0.40	50.57	37.37	2.9	0.4	
4	1	-14.13	-13.24	-12.59	0.41	51.06	37.94	3.2	0.4	
5	1	-13.73	-13.31	-12.72	0.29	50.33	38.13	8.2	2.2	
6	1	-14.32	-13.61	-12.98	0.40	50.67	37.86	5.1	0.3	
7	3	-14.09	-13.67	-13.05	0.36	50.52	38.06	6.7	0.4	
8	4	-14.85	-14.08	-13.42	0.44	50.11	36.85	2.7	4.8	
9	5	-14.16	-13.36	-12.71	0.41	51.01	37.99	3.8	0.2	
10	5	-14.32	-13.51	-12.89	0.34	50.76	37.66	3.3	0.2	
11	25	-14.53	-14.14	-13.53	0.34	50.02	37.25	5.3	0.7	
12	3	-14.64	-13.76	-13.13	0.37	50.57	37.49	3.4	0.3	
13	6	-14.45	-13.23	-12.59	0.40	51.17	37.61	2.0	0.4	
14	3	-14.95	-14.06	-13.42	0.41	50.32	37.26	3.5	0.4	
15	6	-14.78	-13.93	-13.29	0.39	50.38	37.26	3.2	0.5	
16	6	-14.66	-13.86	-13.23	0.39	50.33	37.15	2.9	1.0	
17	25	-14.50	-14.61	-13.96	0.41	49.03	37.61	14.0	4.3	
18	25	-14.03	-14.07	-13.41	0.44	50.11	38.23	10.1	0.7	
19	7	-14.53	-13.71	-13.07	0.40	50.60	37.62	4.1	0.3	
20	25	-14.14	-14.13	-13.43	0.55	50.29	38.36	9.6	0.6	
21	3	-15.00	-14.46	-13.79	0.45	49.79	37.26	6.4	0.9	
22	26	-14.23	-13.65	-13.03	0.35	50.47	37.65	5.1	0.8	
23	7	-14.38	-13.56	-12.89	0.46	50.64	37.57	3.5	0.8	
24	7	-14.62	-13.47	-12.82	0.42	50.89	37.28	1.4	0.7	
25	8	-14.97	-14.47	-13.79	0.49	49.84	37.07	5.4	2.3	
26	9	-14.71	-14.06	-13.33	0.59	50.45	37.96	6.6	1.5	
27	10	-14.89	-14.08	-13.41	0.46	50.38	37.57	5.2	1.4	$_{\mathrm{Bn}}$
28	9	-14.73	-13.64	-12.98	0.42	50.77	37.61	3.0	0.7	
29	11	-14.43	-13.70	-13.08	0.36	50.57	37.25	2.6	0.8	
30	11	-13.86	-13.46	-12.85	0.34	50.64	37.90	5.5	0.8	

TABLE 8—Continued

N	Group	log B5 (ergs cm ⁻²	$ \log H\beta (ergs cm-2 $	$\log H\alpha$ $(ergs cm^{-2})$	$E(B-V)_g$ (mag)	$\log N_{ m Lyc} \ ({ m photons~s}^{-1})$	$\log L_{\rm B5}$ $({\rm ergs \ s^{-1}})$	Age (Myr)	$\sigma(age)$ (Myr)	Note
(1)	(2)	$s^{-1} \mathring{A}^{-1}$) (3)	s^{-1}) (4)	s^{-1}) (5)	(6)	(7)	$\stackrel{\text{A}^{-1}}{(8)}$	(9)	(10)	(11)
31	12	-13.58	-13.16	-12.53	0.37	50.93	38.33	6.1	0.4	
32	23	-13.92	-13.45	-12.83	0.35	50.71	37.72	3.9	0.6	
33	27	-14.66	-13.82	-13.19	0.38	50.41	36.66	< 0.0	3.2	
34	13	-14.22	-13.36	-12.71	0.41	50.98	37.75	2.8	0.6	
35	14	-14.69	-14.05	-13.37	0.50	50.33	37.70	6.0	2.8	$_{\mathrm{Bn}}$
36	23	-13.94	-13.54	-12.89	0.44	50.71	38.01	5.7	0.5	
37	24	-13.29	-12.74	-12.09	0.43	51.55	38.84	5.6	0.5	
38	15	-14.44	-13.61	-12.99	0.36	50.54	37.13	2.4	0.8	
39	15	-14.43	-13.62	-12.99	0.38	50.59	37.37	2.9	0.5	
40	16	-14.26	-13.59	-12.94	0.42	50.57	37.55	3.8	0.7	
41	16	-14.35	-13.32	-12.68	0.41	51.05	37.63	2.3	0.3	
42	16	-13.93	-13.21	-12.61	0.30	50.97	37.96	3.9	0.3	
43	16	-14.49	-13.54	-12.92	0.36	50.73	37.32	2.4	0.5	
44	22	-15.16	-14.11	-13.53	0.28	50.08	36.81	2.7	0.9	
45	28	-13.80	-14.13	-13.62	0.12	49.40	37.57	10.7	3.4	
46	16	-13.59	-13.11	-12.55	0.23	50.73	38.01	5.6	0.8	
47	17	-14.54	-13.62	-13.00	0.36	50.66	37.50	3.0	0.4	
48	17	-13.80	-13.18	-12.59	0.30	50.08	37.50	6.2	8.1	
49	17	-14.70	-13.53	-12.91	0.34	50.78	37.30	2.2	0.3	
50	17	-14.94	-13.77	-13.16	0.32	50.52	37.06	2.2	0.3	
51	18	-14.55	-13.99	-13.31	0.49	50.29	37.07	2.8	4.0	
52	19	-13.97	-13.71	-12.96	0.64	51.09	38.95	8.4	2.9	$_{ m Un}$
53	19	-15.08	-14.72	-13.79	1.03	50.29	38.54	11.3	1.9	$_{ m Un}$
54	19	-14.94	-14.38	-13.48	0.96	50.57	38.56	8.9	2.0	$_{ m Un}$
55	20	-14.86		-14.31					0.5	Bx
56	21	-14.66	-14.10	-13.22	0.93	51.11	38.66	6.7	0.5	$_{\mathrm{Bn}}$
57	21	-14.42	-14.03	-13.06	1.12	51.47	39.29	8.3	0.4	$_{ m Bn}$

TABLE 9
CORRESPONDANCE OF LARGE AND SMALL APERTURES

Large Aperture			Small Apertures	
Number	Age (Myr)	Numbers	Ages (Myr)	$E(B-V)_s^{\ a}$
1	4.6	26 28	6.6 3.0	0.25 0.17
2	4.5	19 23 24	$4.1\ 3.5\ 1.4$	$0.16\ 0.19\ 0.17$
3	5.8	35	6.0	0.21
4	3.8	13 16	2.0 2.9	0.16 0.16
5	3.1	2	2.4	0.18
6	2.8	1 3	$2.3 \ 2.9$	0.18 0.16
7	6.4	5	8.2	0.11
8	5.2	47 48 49 50	3.0 6.2 2.2 2.2	$0.15\ 0.12\ 0.14\ 0.13$
9	5.7	6	5.1	0.16
10	6.9	29 30	2.6 5.5	0.140.14
11	6.1	$32\ 33\ 34$	$3.9\ 0-\ 2.8$	$0.14\ 0.15\ 0.17$
12	5.4	38 39	2.4 2.9	$0.14\ 0.15$
13	4.7	4	3.2	0.17
14	6.1	31	6.1	0.15
15	8.3	17 18 20	$14.0\ 10.1\ 9.6$	$0.17\ 0.18\ 0.23$
16	5.9	36 37	5.7 5.6	0.18 0.18
17	5.3	9 10	3.8 3.3	0.17 0.14
18	6.4	40 41 42 43 45 46	$3.8\ 2.3\ 3.9\ 2.4\ 10.7\ 5.6$	$0.17\ 0.17\ 0.12\ 0.14\ 0.04\ 0.09$
19	6.2	7	6.7	0.14
20	5.6	27	5.2	0.19
21	6.7	52	8.4	0.27
22	5.8	56 57	6.7 8.3	0.39 0.48

^aStellar reddening = $0.44E(B-V)_g$, which is the reddening of the associated gas (§2.3); for comparison, the $E(B-V)_s$ corresponding to $E(B-V)_g = 0.40$ within NGC 4449 is 0.18.